Springer

Acta Mechanica Sinica

CrossMark click for updates

• RESEARCH PAPER •

Acta Mech. Sin., Vol. 41, 423468 (2025)
https://doi.org/10.1007/s10409-023-23468-x

Experimental study of postcritical deformation stage realization in layered composites during tension using digital image correlation and acoustic emission

Valeriy Wildemann, Elena Strungar*, Dmitrii Lobanov, Artur Mugatarov, and Ekaterina Chebotareva

Center of Experimental Mechanics, Perm National Research Polytechnic University, Perm 614990, Russian Federation

Received October 31, 2023; accepted November 26, 2023; published online September 13, 2024

Creating conditions to implement equilibrium processes of damage accumulation under a predictable scenario enables control over the failure of structural elements in critical states. It improves safety and reduces the probability of catastrophic behavior in case of accidents. Equilibrium damage accumulation in some cases leads to a falling part (called a postcritical stage) on the material's stress-strain curve. It must be taken into account to assess the strength and deformation limits of composite structures. Digital image correlation method, acoustic emission (AE) signals recording, and optical microscopy were used in this paper to study the deformation and failure processes of an orthogonal-layup composite during tension in various directions to orthotropy axes. An elastic-plastic deformation model was proposed for the composite in a plane stress condition. The evolution of strain fields and neck formation were analyzed. The staging of the postcritical deformation process was described. AE signals obtained during tests were studied; characteristic damage types of a material were defined. The rationality and necessity of polymer composites' postcritical deformation stage taken into account in refined strength analysis of structures were concluded.

Experimental mechanics, Digital image correlation method, Acoustic emission, Postcritical deformation, Polymer composite

Citation: V. Wildemann, E. Strungar, D. Lobanov, A. Mugatarov, and E. Chebotareva, Experimental study of postcritical deformation stage realization in layered composites during tension using digital image correlation and acoustic emission, Acta Mech. Sin. 41, 423468 (2025), https://doi.org/10.1007/s10409-023-23468-x

1. Introduction

Prediction of failure processes, evaluation of durability and safety of structures made of polymer composites require studies of damage accumulation during deformation processes [1-3]. They lead to a non-linear behavior on stress-strain curves [4-6]. Moreover, if structural defects are sufficiently developed, the postcritical stage (also called the necking stage or softening stage) may be implemented, characterized by stress reduction during strain increase [7-10]. Various areas of this stage correspond to certain damage mechanisms. Their understanding allows predicting the composite's behavior under various loading conditions using computational methods [11-14].

The postcritical stage occurs in various materials: metals [15,16], rocks [17,18], and concretes [19-23]. Besides, the postcritical strain stage is taken into account in many cohesive zone models [24-26]. The softening stage is observed in polymer composites when the matrix is predominantly deformed [25-29]. Particular interest is to study the behavior of layered composites during in-plane shear [30-33].

Postcritical deformation of metals is accompanied by significant plastic deformations, which lead to localization in the form of a neck on the specimen work part. This phenomenon greatly complicates the stress-strain curve obtaining and data recorded in experiments interpretation.

*Corresponding author. E-mail address: cem.spaskova@mail.ru (Elena Strungar)
Executive Editor: Zhong Zhang

Experimental and theoretical studies of strain localization in the neck give an insight into physical and mechanical processes resulting in failure [34,35]. Few papers are dedicated to the neck investigation in composites [36,37].

To study specific features of material deformation in the presence of heterogeneous strain fields, various modern analysis systems can be used. Many researchers prefer visual image correlation three-dimensional (VIC-3D) contactless optical video systems more than strain gauges due to their ability to obtain displacements and strain fields all over the sample surface [32,38,39]. The VIC-3D was used to study the elastic-plastic deformation of polymer composites in Refs. [40-44].

The postcritical deformation stage is caused by multiple damage accumulation in the material structure. Hence, the acoustic emission (AE) signal recording method, based on the recording of elastic waves occurring in deformation and local restructuring, is reasonable to use in damage determination, especially in polymer composites [45-47]. The AE method allows the investigation of damage accumulation processes and the definition of optimal test parameters (such as strain rate, and frequency), which have a significant influence on failure processes. This method provides a more accurate evaluation of composite materials' behavior and prevention of possible accidents [48-52]. However, a small number of papers are dedicated to the composites' postcritical stage study with AE signals recording [36].

This paper represents an experimental study of postcritical deformation regularities of carbon-fiber reinforced plastic with orthogonal layup. Tension tests were carried out on specimens cut out in various directions. Stress-strain curves were built, showing that the postcritical stage implements during in-plane shear. An elastic-plastic model based on the deformation plasticity theory was proposed for the considered composite taking into account the identified regularities. The optical video system was used to analyze the evolution of heterogeneous strain fields and the neck formation process. The AE signal recording method found characteristic defects taking place during deformation processes. A conclusion was made on the necessity and rationality of studying the postcritical deformation stage of polymer composites.

2. Material and methods

To manufacture specimens, a plate was made by autoclave molding ($h \approx 2$ mm thick) composed of 16 layers of prepreg carbon fiber VKU-60 (VIAM, Russian Federation) based on carbon fabric and epoxy binder. The specimens $L \approx 150$ mm long and $b \approx 23$ mm wide (the gage length 50 mm, grip parts 50 mm) were cut from this plate using Zund GL-2500 plotter in two directions: along carbon threads (Type-0) and at 45° to them (Type-45).

Experimental studies were carried out using the large-scale research facilities "Complex of testing and diagnostic equipment for studying properties of structural and functional materials under complex thermomechanical loading" at the Center of Experimental Mechanics of the Perm National Research Polytechnic University (PNRPU).

The tension tests were carried out using Instron 5982 (±100 kN) electromechanical testing system by loading at a constant movable grip rate of 2 mm min^{-1}, together with the VIC-3D optical strain field and movement analysis video system and AMSY-6 AE signal recording system. Testing and measurement systems were synchronized during tests using NI USB-6251 16-bit high-rate analog to digital converter (ADC) unit.

The deformation process was recorded using two Prosilica 50 mm cameras (4872 × 3248, 16 Mp). The frame frequency was 3 fps. VIC-3D software enables using various correlation criteria for mathematical evaluation of digital image correspondence. We used the criterion of standardized sum of squares of differences with zero mean since it is the least sensitive to illumination changes during tests, which ensures the best combination of time frames and accuracy of results. The Lagrange finite strain tensor was used during post-processing for calculations. *Oy* axis was directed along the specimen (along the loading axis), and *Ox* was perpendicular to the loading axis in the specimen plane. An additional software module "virtual extensometer" was used in loading and stress-strain curves construction to track mutual movement between two points on the specimen surface.

The accuracy of the contactless optical system is defined by the specifications of lenses and digital cameras, namely, the matrix sensitivity, resolution, and permitted frame frequency. The specimen surface, camera configuration, and calibration also affect the resulting experimental data. According to the tests carried out in Ref. [53], a conclusion was made that the VIC-3D system can obtain displacements with an accuracy comparable to that of the strain gauges, with the possible deviation from the true value about 0.15%.

AE signals were recorded by the Vallen AMSY-6 system. To record signals, we used AE144A and AE105A wide-band sensors with frequency bands of 100-500 and 450-1150 kHz, respectively, with a pre-amplifier with an amplification coefficient of 34 dB. The sensors were attached to the specimen using a fastening system. The data sampling frequency was 10 kHz, the threshold value of AE signal recording was 40 dB. The energy parameter, AE signal duration, spectral maximum frequency, and peak amplitude were used as informative parameters (characteristics of fast Fourier transform). The energy parameter of AE signals was calculated using a special software option in energy units (eu), 1 eu = 10^{-18} J. After tension tests the

samples' surfaces were analyzed using CarlZeiss SteREO Discovery.V12 (ZEN software) digital stereo microscope.

Tension tests of Type-0 and Type-45 specimens were carried out according to ASTM D3039 and ASTM D3518, respectively. Longitudinal strains ε_{yy} and transverse strains ε_{xx} were calculated using the "virtual extensometer" tool. Loading diagrams (axial loading P dependence on displacement u) and stress-strain curves (normal (tangential) stress σ (τ) dependence on longitudinal (shear) strains ε (γ)) were built. Elastic characteristics of the composite material were identified (Young's modulus E, Poisson ratio ν, shear modulus G). Stress-strain curves were also built using true stresses σ_{true} (τ_{true}) to take into account the changes in the cross-section area. We assumed that the change in thickness could be neglected, therefore, true stresses were calculated according to the formula

$$\sigma_{\text{true}} = \frac{P}{hb(1+\varepsilon_{xx})}, \quad \tau_{\text{true}} = \frac{P}{2hb(1+\varepsilon_{xx})}. \tag{1}$$

The investigation is limited by experimental regularities obtaining and model building on their basis. Stress-strain curves were introduced to simplify the composite's mechanical behavior presentation (considered as homogeneous material, allowing the model building). Registration of strains was carried out using an additional module of VIC-3D software "virtual extensometer". The main advantages of using the "virtual extensometer" are non-contact registration of deformations, no mechanical impact on the surface of the specimen, and the possibility of using several "virtual extensometers" on one specimen, both in longitudinal and transverse directions, which leads to an increase in the accuracy of the recorded deformations. The disadvantage of VIC-3D is the partial loss of data associated with the delamination of the applied the surface paint. Only two variants of specimens' orientation were considered: along the carbon threads and at 45° to them. We assume that the composite's behavior is independent of the strain rate, so all the loadings are static. According to many studies, such as Refs. [54,55], we relate the peak frequency ranges to the certain fracture mechanisms. Low frequencies correspond to matrix cracking, medium frequencies to delamination, and high frequencies to fiber fracture.

3. Results and discussions

3.1 Loading diagrams and stress-strain curves

Loading diagrams of Type-0 and Type-45 specimens were built using the test system data (built-in displacement sensor) and the video system data (Fig. 1). The initial part of Type-0 samples loading curves built without VIC-3D data has a non-linear section. This peculiarity is explained by the mutual displacement of test machine parts previously being

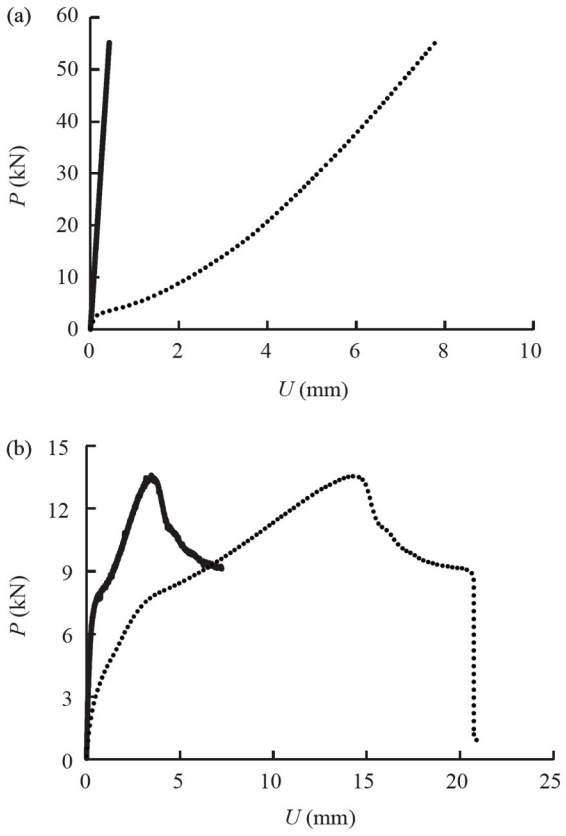

Figure 1 Loading curves built using built-in displacement sensor (dotted line) and VIC-3D data (solid line): (a) for the samples of Type-0; (b) for the samples of Type-45.

in a non-loaded state. A significant difference in displacements with equal loads was caused by not only the change in displacement measurement tool but also the rigidity of the testing machine. Therefore, the difference in displacements was lower for Type-45 specimens than for Type-0 specimens (the first ones were significantly less rigid). On the other hand, the loading diagrams obtained with VIC-3D were less complete due to paint spalling during the softening process.

Figure 2 presents the stress-strain curves (a) and (c) and the dependencies of transverse strain on longitudinal strain for Type-0 specimen tests (b). The stress-strain curves for Type-45 specimens (in-plane shear) were built in true and engineering stresses. The deviation between true and engineering stresses for Type-0 specimens was below 0.3 MPa.

The average Young's modulus was 65.2±1.4 GPa, the Poisson coefficient was 0.075±0.016, the shear modulus was 4.42±0.09 GPa. Different mechanical behavior was noted during tension along reinforcement threads and at 45° to them. In the first case, the failure occurred in an elastic-brittle manner (linear deformation until failure and no residual strains). It is explained by the most of the load is taken by the reinforcement fibers, whose behavior is linear-elastic up to the destruction moment. The fracture of several threads induces the nonequilibrium failure process and sharp

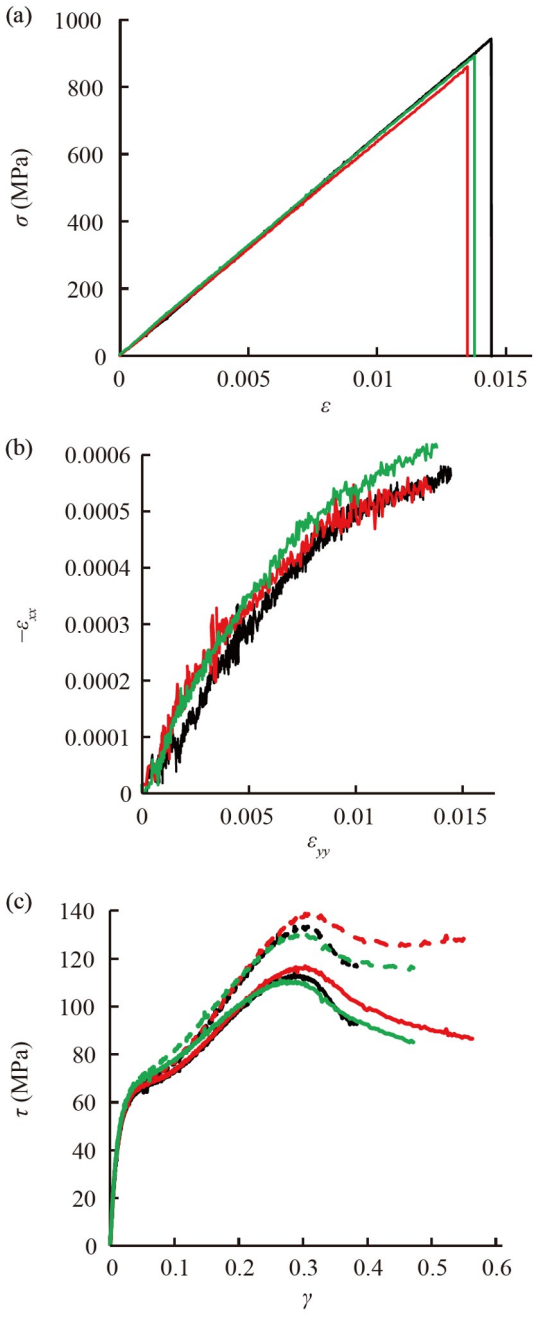

Figure 2 Composite's stress-strain curves: (a) along the reinforcement; (b) corresponding dependencies of transverse strains on longitudinal ones; (c) during in-plane shear in engineering (solid lines) and true (dashed lines) stresses.

load drop. In the second case, the postcritical deformation stage was implemented, even when the stress-strain curve was built using true stresses. This happens because the external load is taken by the matrix during in-plane shear. The matrix behavior can be elastic-plastic, moreover, multiple matrix cracking occurs, causing many slight load drops, summarizing into the external load's falling and postcritical deformation implementation. The previous study [36] confirms that the composite's behavior can be elastic-plastic during in-plane shear. Moreover, the relationship between transverse and longitudinal strains was non-linear, reflecting the change in the Poisson ratio. These peculiarities must be taken into account in functions defining the mechanical behavior of the material.

Thus, according to the test results, it can be noted that the stacking scheme affects the degree of realization of the subcritical stage of deformation. Also, according to the previously obtained results, it can be noted that the realization of the subcritical stage of deformation depends on the geometry of the specimens, in particular, the length of the working part (i.e., the stiffness of the loading system [28]). Also, the influence of the loading rate on the realization of the subcritical stage of deformation is shown in Ref. [29].

3.2 Orthogonal-layup composite's elastic-plastic model

Elastic-plastic model for orthogonal-layup composite in plane stress state can be written as a relationship between strains ε_{11}, ε_{22} and γ_{12} with stresses σ_{11}, $\sigma_{22,}$ and τ_{12} using compliance coefficients s_{ij}^0 [56]. In the coordinate system related to orthotropy axes (with the directions of reinforcement threads):

$$\begin{Bmatrix}\varepsilon_{11}\\ \varepsilon_{22}\\ \gamma_{12}\end{Bmatrix}=\begin{bmatrix}s_{11}^0 & s_{12}^0 & 0\\ s_{12}^0 & s_{22}^0 & 0\\ 0 & 0 & s_{66}^0\end{bmatrix}\begin{Bmatrix}\sigma_{11}\\ \sigma_{22}\\ \tau_{12}\end{Bmatrix}. \tag{2}$$

Let us note that the compliance coefficients may depend on the type of the stress-strain state. Therefore, they are functions, whose definition requires a set of standard tests. When the coordinate system rotates in the plane of layers to angle φ strain-stress relationship will look as follows:

$$\begin{Bmatrix}\bar{\varepsilon}_{11}\\ \bar{\varepsilon}_{22}\\ \bar{\gamma}_{12}\end{Bmatrix}=\begin{bmatrix}\bar{s}_{11} & \bar{s}_{12} & \bar{s}_{16}\\ \bar{s}_{12} & \bar{s}_{22} & \bar{s}_{26}\\ \bar{s}_{16} & \bar{s}_{26} & \bar{s}_{66}\end{bmatrix}\begin{Bmatrix}\bar{\sigma}_{11}\\ \bar{\sigma}_{22}\\ \bar{\tau}_{12}\end{Bmatrix}. \tag{3}$$

The changed compliance coefficients are found using the formulas below (designations for simplification are $s\to\sin\varphi$, $c\to\cos\varphi$:

$$\begin{aligned}
\bar{s}_{11}&=c^4s_{11}^0+s^4s_{22}^0+\left(2s_{12}^0+s_{66}^0\right)s^2c^2,\\
\bar{s}_{12}&=\left(s^4+c^4\right)s_{12}^0+\left(s_{11}^0+s_{22}^0-s_{66}^0\right)s^2c^2,\\
\bar{s}_{16}&=\left[2c^2s_{11}^0-2s^2s_{22}^0+\left(2s_{12}^0+s_{66}^0\right)\left(s^2-c^2\right)\right]sc,\\
\bar{s}_{22}&=s^4s_{11}^0+c^4s_{22}^0+\left(2s_{12}^0+s_{66}^0\right)s^2c^2,\\
\bar{s}_{26}&=\left[2s^2s_{11}^0-2c^2s_{22}^0-\left(2s_{12}^0+s_{66}^0\right)\left(s^2-c^2\right)\right]sc,\\
\bar{s}_{66}&=\left(s^2-c^2\right)^2s_{66}^0+\left(4s_{11}^0+4s_{22}^0-8s_{12}^0\right)s^2c^2.
\end{aligned} \tag{4}$$

In a particular case when the rotation angle $\varphi = 45°$:

$$\begin{aligned}
&\bar{s}_{11} = \bar{s}_{22} = \frac{1}{4}\left(s_{11}^0 + s_{22}^0 + 2s_{12}^0 + s_{66}^0\right),\\
&\bar{s}_{12} = \frac{1}{4}\left(s_{11}^0 + s_{22}^0 + 2s_{12}^0 - s_{66}^0\right),\\
&\bar{s}_{16} = \bar{s}_{26} = \frac{1}{2}\left(s_{11}^0 - s_{22}^0\right),\\
&\bar{s}_{66} = s_{11}^0 + s_{22}^0 - 2s_{12}^0.
\end{aligned} \tag{5}$$

We can write these equations for the tension tests in various directions. For the tension along the reinforcement threads (along the orthotropy axis x_1):

$$\begin{cases}
\varepsilon_{11} = s_{11}^0 \sigma_{11},\\
\varepsilon_{22} = s_{12}^0 \sigma_{11} = \dfrac{s_{12}^0}{s_{11}^0}\varepsilon_{11},\\
\gamma_{12} = 0.
\end{cases} \tag{6}$$

Therefore, the damage functions reflecting the change in compliance coefficients s_{11}^0 and s_{12}^0 can be obtained from the uniaxial tension test along the reinforcement direction using the dependencies between the normal stress σ_{11} and longitudinal strain ε_{11} and between transverse strain ε_{22} and ε_{11}. For the composite considered in this paper, the directions x_1 and x_2 are equal (the fabric is equally strong), so the functions s_{11}^0 and s_{22}^0 are also equal, and no additional test is required. In case of tension at 45° to the direction of reinforcement threads (in-plane shear):

$$\begin{cases}
\bar{\varepsilon}_{11} = \bar{s}_{11}\bar{\sigma}_{11} = \dfrac{1}{4}\left(s_{11}^0 + s_{22}^0 + 2s_{12}^0 + s_{66}^0\right)\bar{\sigma}_{11},\\
\bar{\varepsilon}_{22} = \bar{s}_{12}\bar{\sigma}_{11} = \dfrac{1}{4}\left(s_{11}^0 + s_{22}^0 + 2s_{12}^0 - s_{66}^0\right)\bar{\sigma}_{11},\\
\bar{\gamma}_{12} = \bar{s}_{16}\bar{\sigma}_{11} = \dfrac{1}{2}\left(s_{11}^0 - s_{22}^0\right)\bar{\sigma}_{11}.
\end{cases} \tag{7}$$

Converting of Eq. (7) lead to

$$\bar{\varepsilon}_{11} - \bar{\varepsilon}_{22} = s_{66}^0 \frac{\bar{\sigma}_{11}}{2}. \tag{8}$$

Therefore, the third damage function can be obtained from a standard static ±45° tension test.

Based on the above, to describe the deformation processes of the layered composite considered in this paper, it is enough to know three damage functions found from two standard tests. The material behaves as the elastic-brittle while tension along the reinforcement direction, so the damage function is piecewise constant (0 until the failure moment and 1 after it). In accordance with Ref. [7], three damage functions ω_E, ω_{ν} and ω_G can be defined as

$$\begin{cases}
\sigma_{11}(\varepsilon_{11}) = E_1\left(1 - \omega_E(\varepsilon_{11})\right)\varepsilon_{11} \Leftrightarrow \omega_E(\varepsilon_{11}) = 1 - \dfrac{\sigma_{11}(\varepsilon_{11})}{E_1\varepsilon_{11}},\\
-\varepsilon_{22}(\varepsilon_{11}) = \nu\left(1 - \omega_\nu(\varepsilon_{11})\right)\varepsilon_{11} \Leftrightarrow \omega_\nu(\varepsilon_{11}) = 1 + \dfrac{\varepsilon_{22}(\varepsilon_{11})}{\nu\varepsilon_{11}},\\
\tau_{12}(\gamma_{12}) = G\left(1 - \omega_G(\gamma_{12})\right)\gamma_{12} \Leftrightarrow \omega_G(\gamma_{12}) = 1 - \dfrac{\tau_{12}(\gamma_{12})}{G\gamma_{12}}.
\end{cases} \tag{9}$$

Therefore, compliance coefficients are defined as

$$\begin{cases}
s_{11}^0 = \dfrac{1}{E_1(1-\omega_E)},\\
s_{12}^0 = \dfrac{\nu(1-\omega_\nu)}{E_1(1-\omega_E)},\\
s_{66}^0 = \dfrac{1}{G(1-\omega_G)}.
\end{cases} \tag{10}$$

Examples of damage functions obtained in the experiment are represented in Fig. 3. It seems reasonable to use them to predict the mechanical behavior of composites with other reinforcement schemes.

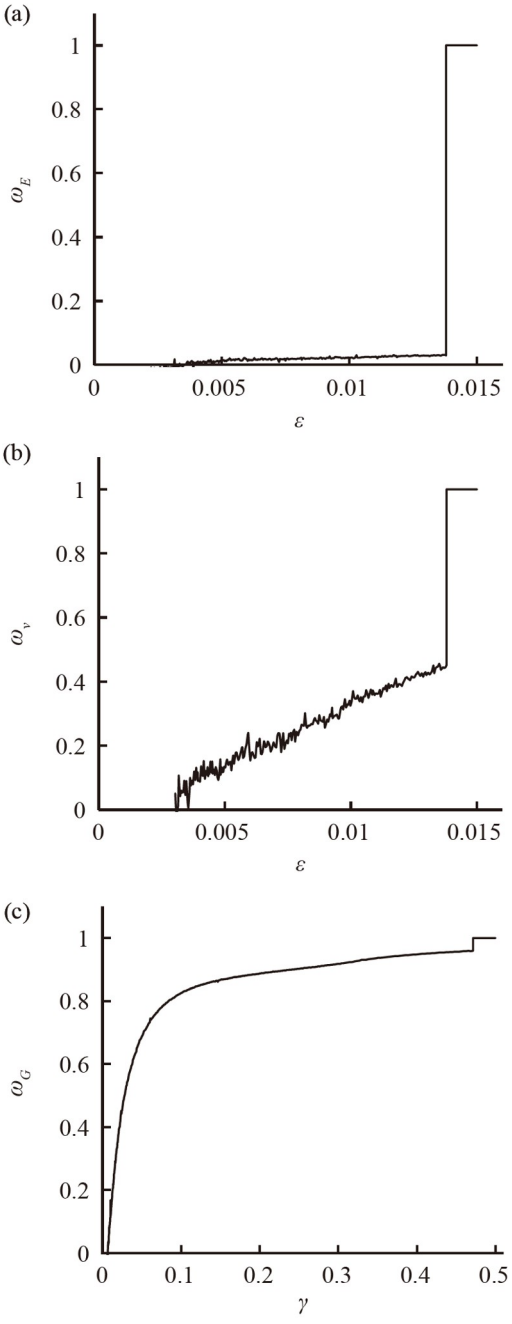

Figure 3 Experimental damage functions: (a) ω_E; (b) ω_ν; (c) ω_G.

3.3 Inhomogeneous strain field analysis

During Type-45 specimen tests, the non-linear and post-critical deformation was accompanied by localization in the form of the neck. Therefore, it is necessary to study the material's behavior in various specimen zones. For this purpose, the "virtual extensometers" were installed further away from the neck zone (E0), at the failure site along the neck (E1), and at both specimen areas (E2). We built three stress-strain curves using these extensometers (Fig. 4). Up to the shear strength reaching, all stress-strain curves were similar. Hence, the deformation process of the material in the entire specimen volume was relatively homogeneous. After neck formation, the material in the E0 area was unloaded (only the elastic part of strains decreased) during external load reduction. At the same time, material in the neck part (E1) showed postcritical behavior, resulting in a long falling part on the stress-strain curve. The intermediate stress-strain curve was obtained by using E2 extensometer. Thus, we recommend building the composite stress-strain curve by measuring strains in the neck zone. A disadvantage of this method is a partial loss of data related to the spalling of paint applied on the specimen surface. To solve this issue, more viscous paints are recommended. It also must be noted that specimen parts distanced from the neck act as part of the loading system during softening process, significantly affecting the stability of the postcritical deformation process [36]. Therefore, it is relevant to develop novel experimental methods to obtain the complete stress-strain curves, probably for specimens with reduced work part.

Figure 5 shows the evolution of the longitudinal strain field ε_{yy} for points 1-8 on the stress-strain curve from Fig. 4. The significant inhomogeneity and strain localization in the form of stripes located along the carbon threads were noted. Moreover, individual spots of strain localization (due to the effects of the braiding structure) and periodicity cells of a certain characteristic size were observed.

The heterogeneous distribution of strains for the Type-0 specimens (Fig. 6) showed that the damages were localized along the entire specimen surface. In places where longitudinal and transverse fibers crossed, areas with inhomogeneous distribution of strain were forming during tension. The observed spots are explained by the fabric structure. If the thread near the sample surface is oriented along the loading direction, the fibers take the most of external load, and local strains are less. On the other hand, if the thread is oriented across the loading direction, the matrix takes the external load, and local strains are large. The periodic structure of the fabric reflects the spots of strain localization observed with the VIC-3D. For the Type-45 specimens, strain fields had an irregular distribution in the form of stripes oriented at 45° to the loading direction (Fig. 6). Destruction started in zones located closer to the specimen center. The strips might also be explained by the fabric's structure features. In the areas between the parallel threads, there is more matrix than the fibers, simplifying the shear between them and causing large strains. However, in the middle of the threads, the matrix concentration is less, so the local strain values decrease.

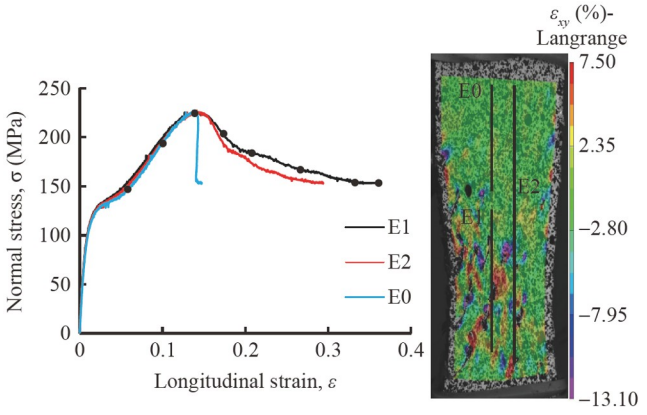

Figure 4 Stress-strain curves constructed using various "virtual extensometers" locations on the specimen surface.

For Type-45 composite specimens, the distribution of ε_{yy} strain is analyzed along the line L (Fig. 7) drawn along the entire specimen. Each curve is represented for points 1-5 on the stress-strain curve from Fig. 4. The Strain diagram had periodic maximums and minimums of shear strain. The maximum difference between strain values in maximum and minimum points was about 60%, while the curves for various load levels were similar and could be easily moved to higher strain levels as the external load increased. The space between neighboring maximums and minimums is aligned with the micro-structure of the composite. For the lower value of the applied load, the strain distribution showed a relatively regular pattern. However, for the later stages of testing, it changed to the periodic strain maximums and minimum distribution in the area of neck formation. While the applied load was further rising, the distribution changed from regular to irregular. These results were obtained using an additional video system tool "line".

3.4 AE signals analysis

Based on the data obtained by the AE signal recording system, the parametric analysis was carried out. Dependencies of the AE signal energy parameter, peak amplitude, peak frequencies of signals, and signal length on time were built and analyzed.

AE signal peak frequencies (Fig. 8) had several characteristic ranges. Since we used sensors with the ranges above 100 kHz, AE signals with the frequency below 100 kHz may be non-representative. However, the usage of two sensors with various bandwidths allowed to expand an overall band up to the 1150 kHz. Signals for the Type-0

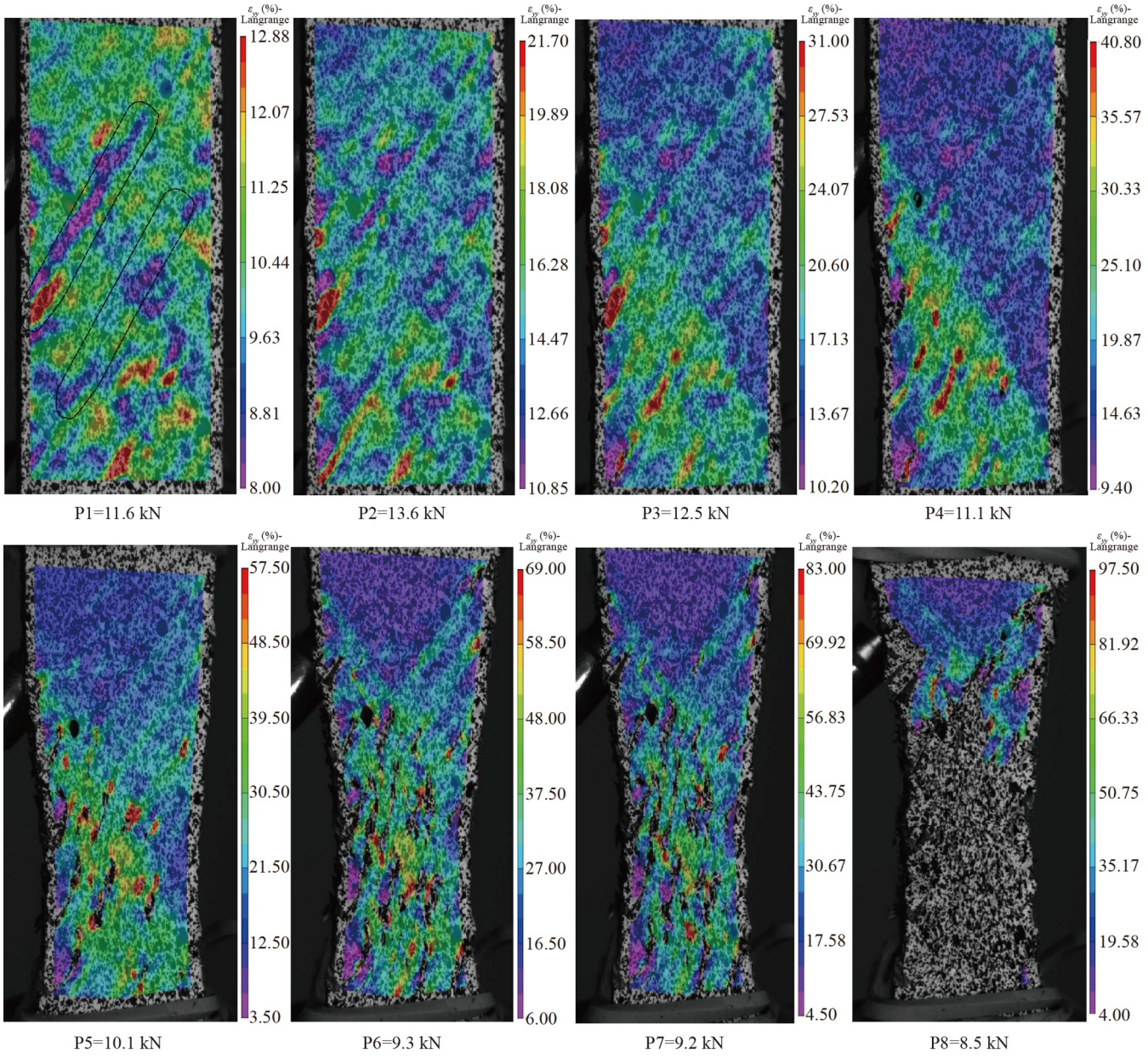

Figure 5 Evolution of ε_{yy} strain fields.

specimens were observed immediately after the test started, which may indicate that this type of specimen had the fiber and matrix destroyed simultaneously. Many signals for both types of specimens were observed in the high-frequency band (from 700 to 900 kHz), which may indicate a multiple fibers break. It can be also noted that the Type-45 specimens had fewer signals within the range from 200 to 450 kHz.

To evaluate AE signals in the postcritical loading stage, peak frequency distribution on the loading curve falling part for the Type-45 specimen was built (Fig. 9). It should be noted that two separate bands can be distinguished in the medium frequency band: 370-400 and 410-570 kHz. It shows that during the postcritical stage material underwent delamination and fiber slippage accompanied by multiple fiber breakages, manifested in the growth of the number of signals in the high-frequency band. From 210 to 230 s no low-frequency signals were detected, which may indicate that the matrix was almost fully fractured by this time. The distribution of AE signals peak frequencies suggests that after matrix failure in the neck area material had multiple delaminations so that fibers started to slip, the matrix and fiber began to work separately, fiber threads and separate fibers were failing.

The dependencies between the relative number of signals and spectral maximum frequencies were built for both specimen types (Fig. 10). The number of signals in each band can be estimated for bands distinguished earlier. The maximum number of signals in both types of specimens was

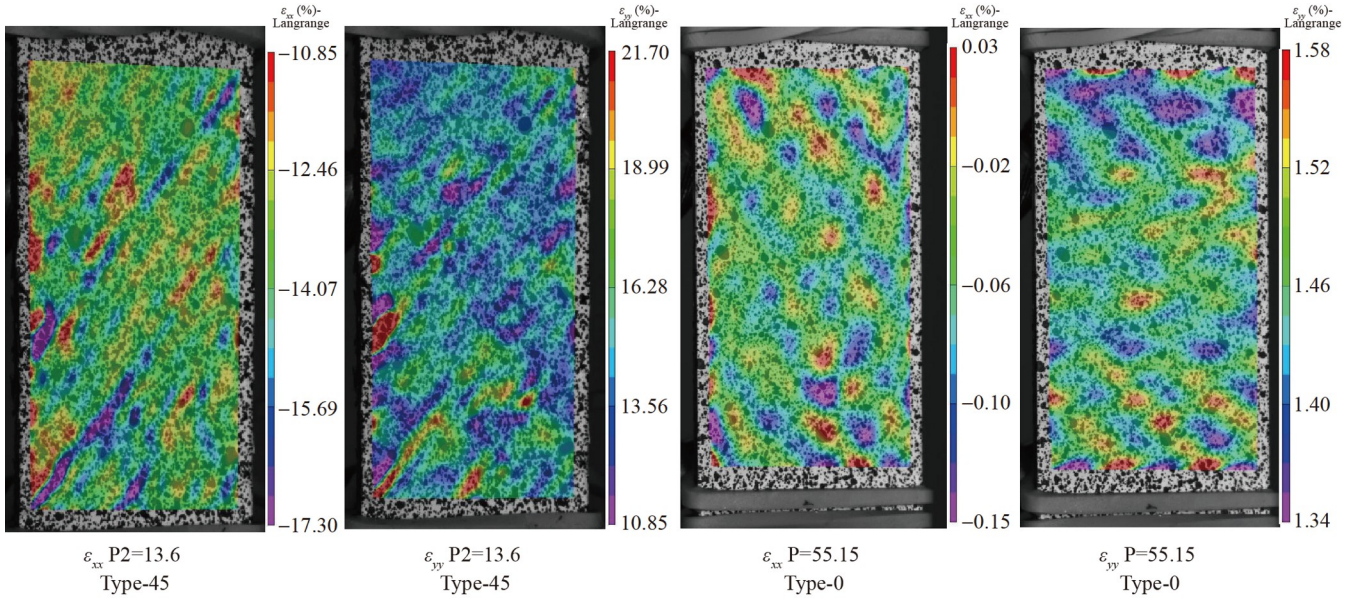

Figure 6 Strain fields for Type-0 and Type-45 specimens at the maximum load value.

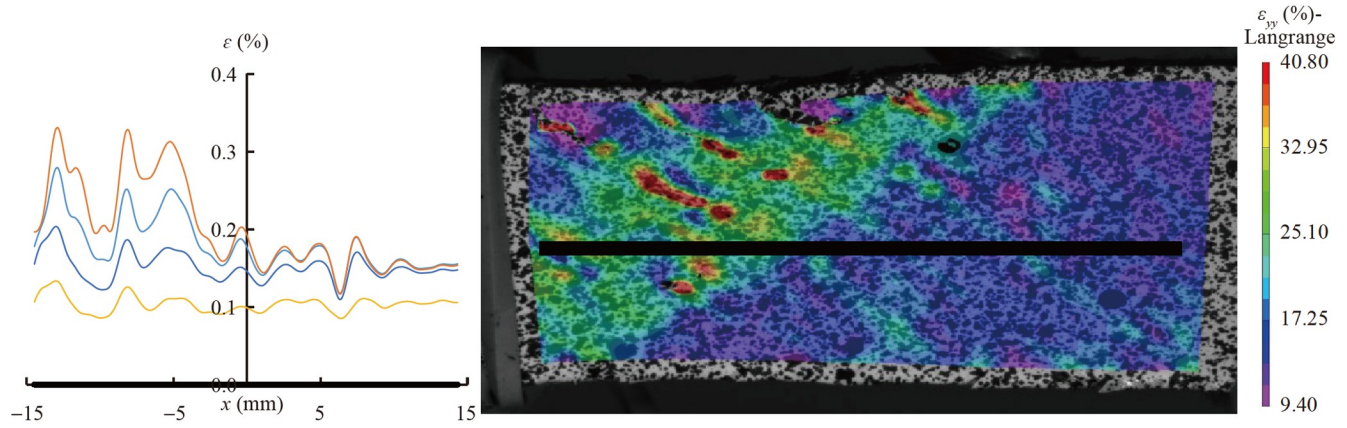

Figure 7 Plots of the ε_{yy} strain distribution along the Type-45 specimen.

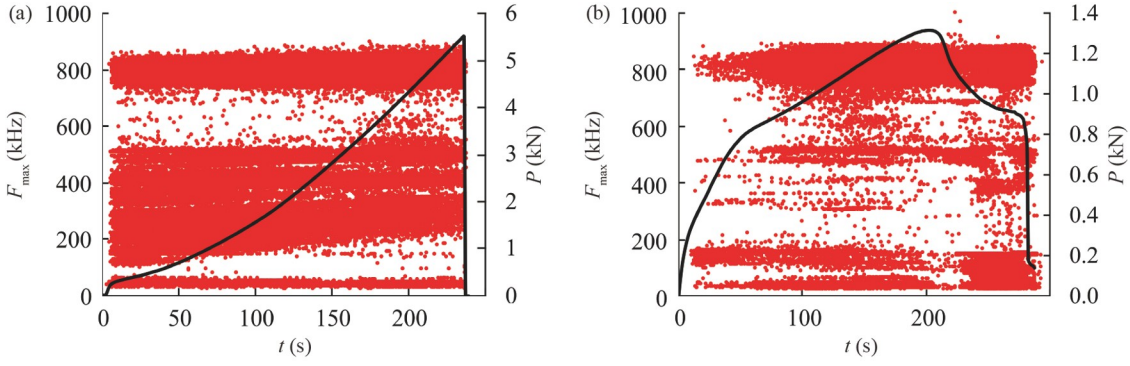

Figure 8 The AE signals peak frequency dependencies on time, combined with the loading diagrams: (a) for the Type-0 specimens; (b) for the Type-45 specimens.

observed in the low frequency band. At the same time, in the high frequency band, almost the same number of signals were recorded. It should be noted that Type-45 specimens had significantly fewer signals recorded in the medium band than Type-0 specimens. According to the analysis of the spectral maximum frequencies, typical bands were dis-

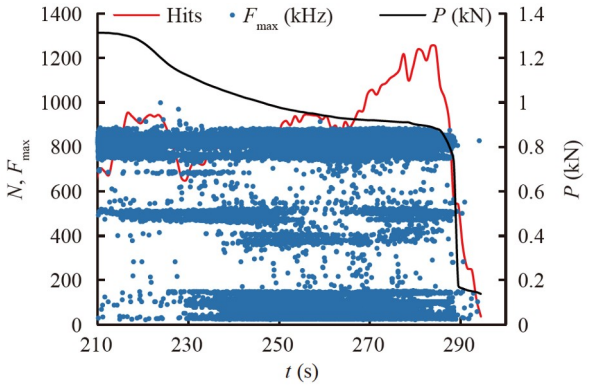

Figure 9 Peak frequencies distribution on the postcritical deformation stage for the Type-45 specimen.

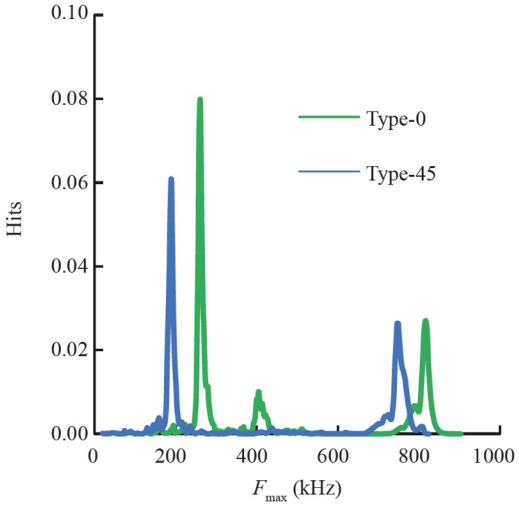

Figure 10 Spectral maximum frequency distribution for Type-0 and Type-45 specimens.

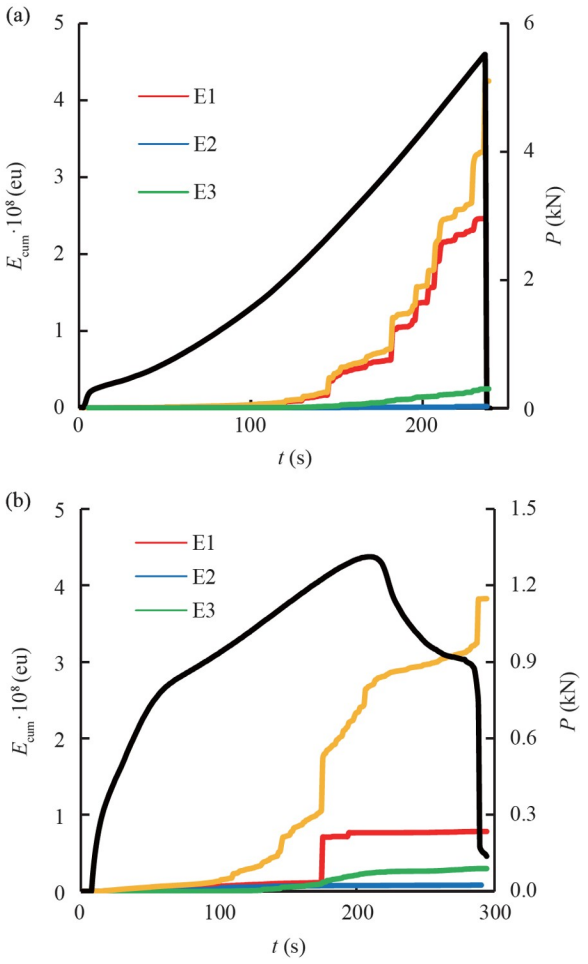

Figure 11 Dependencies of the AE signals cumulative energy on time, combined with the loading diagrams: (a) for the Type-0 specimens; (b) for the Type-45 specimens.

tinguished for each specimen. The other parameters of AE signals were sorted by the identified band ranges.

Figure 11 represents dependencies of AE signals cumulative energy on time. The red line shows energy recorded in the lower frequency band. In both specimen types, it is higher than the energy of the other bands. However, the total cumulative energy in Type-45 specimens is composed not only of energy values in the considered bands. This is caused by an outburst of the signals with high energy beyond the distinguished frequency bands.

The nature of energy outbursts was different in specimens of various types. As the external load was rising in the Type-0 specimen, the signal energy gradually increased, and the energy parameter peak coincided with the maximum load value, followed by the specimen failure. Signals in the Type-45 specimen differ in the energy level to a greater extent. The maximum jump was observed near achieving the maximum load value, but energy parameter outbursts were recorded in the further postcritical stage. One of them, close to the maximum, was recorded at the test end.

It should be noted that the level of cumulative energy in specimens of various types differed insignificantly despite the fact that the maximum load of the Type-0 specimen was more than 3 times higher. After reaching the maximum load and further softening in the Type-45 specimen, the cumulative energy was growing, which showed that the damage accumulation continued until the test ended. Type-45 specimen also showed a more intermittent nature of cumulative energy growth, which indicates that the energy in certain signals differed greatly during loading.

Figure 12 represents the AE signals' peak amplitude dependencies on time, also distributed by characteristic frequency bands. The Type-0 specimen showed the amplitude growth during loading. Signals with the amplitude 75 dB and higher were observed, followed by the maximum peak amplitude achieved at the maximum load value. The Type-45 specimen had the signal amplitude distributed less evenly. After the beginning of the postcritical stage, the signal amplitudes decreased, without reaching the maximum value after the test ended.

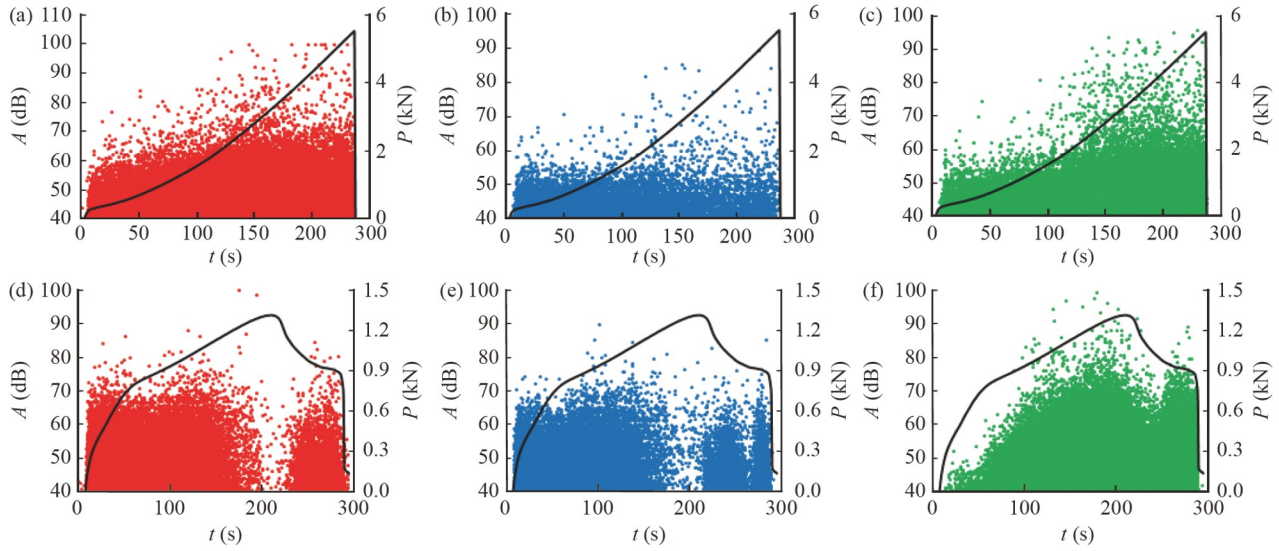

Figure 12 Time dependence of AE signals amplitudes: (a) for the Type-0 specimens in the ranges of low; (b) medium; (c) high frequencies; (d) for the Type-45 specimens in the ranges of low; (e) medium; (f) high frequencies.

From the amplitude of the signals in the selected frequencies, it can be concluded that when the maximum load is reached in specimen Type-45, fibers are predominantly fractured, and the process of fiber fracture starts after the first minute, whereas delamination and matrix cracking are recorded from the beginning of the test. In the Type-0 specimen, the signals corresponding to matrix fracture are recorded throughout the test, while the signals corresponding to fiber fracture increase in amplitude as the maximum load is approached.

The Type-45 specimen had a significant reduction of signal numbers within low and medium frequency ranges in 200-220 s. The signal amplitudes were also low in this time period. However, the amplitudes of the signals in the high frequency band were 75 dB and higher, which shows the presence of multiple fiber failure.

The duration of AE signals was also analyzed in the considered frequency bands. The Type-0 specimens had the signal duration three or more times higher than those recorded for the Type-45 specimens in the same bands (Fig. 13). The results show that in the investigated material signals from the matrix fracture have the maximum duration.

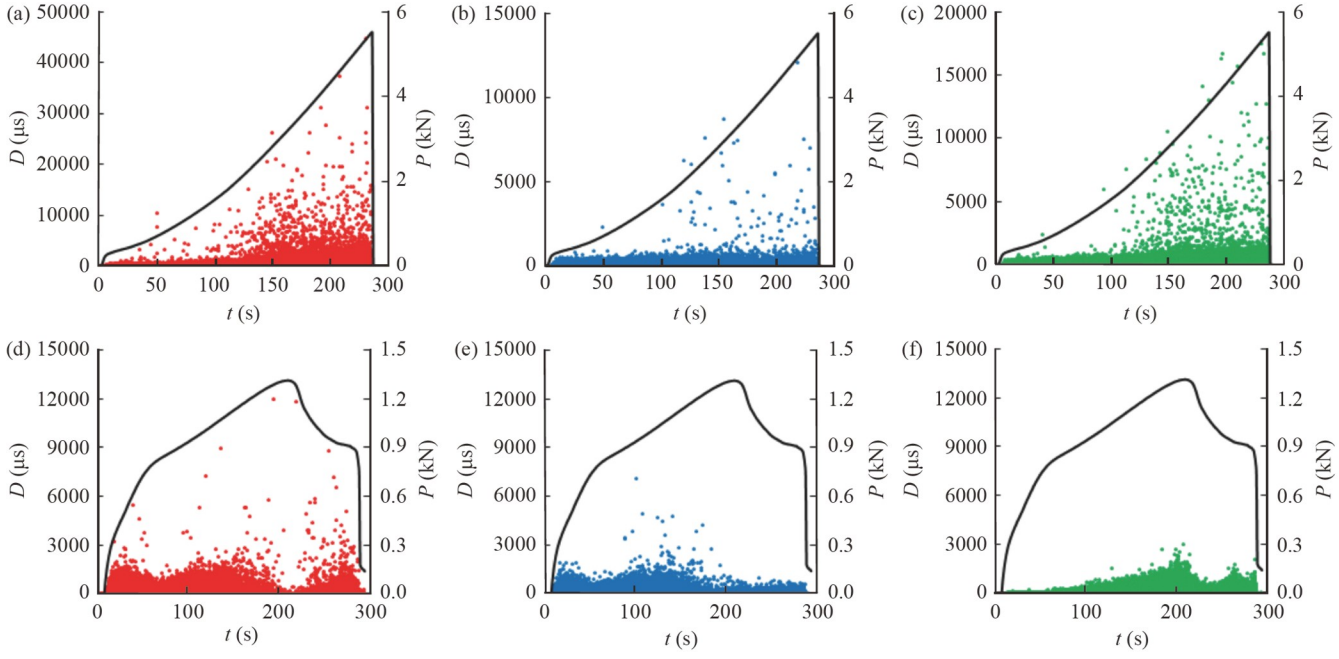

Figure 13 Dependence of the AE signals duration on time: (a) for the Type-0 specimens in the ranges of low; (b) medium; (c) high frequencies; (d) for the Type-45 specimens in the ranges of low; (e) medium; (f) high frequencies.

However, when approaching the maximum load value, the duration of fiber breakage signals in the Type-0 specimen gradually increases and reaches the maximum values before fracture. The signal duration in the Type-45 specimens went down as the spectral maximum frequencies increased. The maximum duration in the Type-0 specimen signals was recorded in the low frequency band, and the minimal one was found in the medium band.

The conclusions made upon the data obtained by the AE method were confirmed by the analysis of the destroyed specimen provided with an optical microscope (Fig. 14). The Type-0 specimen had many destroyed fibers and a fractured matrix, several fibers were layered in the failure zone. The Type-45 specimen had elongated fibers, which were especially clearly seen from the side. The matrix cracking leads to an inter-layer failure and multiple violations of adhesion between carbon threads, followed by the failure of fiber bundles and individual fibers. It can be noted that the angle between threads decreased after testing and became more acute.

4. Conclusions

The results of the layered composite postcritical deformation investigation are presented in this paper. The dependence of mechanical behavior on the tension direction was revealed. Composite behaved as elastic-brittle material along the reinforcement direction, though the presence of a softening stage on the stress-strain curve was found out during tension at the angle of 45° to the carbon threads orientation. For the case of a plane stress state, the novel model of layered composite mechanical behavior was proposed, which assumes the use of three damage functions determined by two standard tests. The analysis of inhomogeneous displacement and strain fields was carried out by the DIC method. The dependence of strain localization nature on reinforcement orientation was observed. The influence of the loading system rigidity on the softening process stability was noted. The analysis of the AE signals recorded during the tests was carried out. Three characteristic ranges of peak frequencies were determined, corresponding to the matrix destruction, adhesion between matrix and fiber violation, and fiber failure. The relationship between the tested sample type and the nature of the distribution of amplitudes, duration, and energy of AE signals was revealed. The typical defects were determined by an optical microscope, confirming the AE signals analysis results. Based on the above, we conclude that the postcritical deformation stage should be taken into account in the structure's strength analysis to ensure reliability and safety. It is important to carry out further investigation of postcritical deformation of layered composites with various reinforcement schemes.

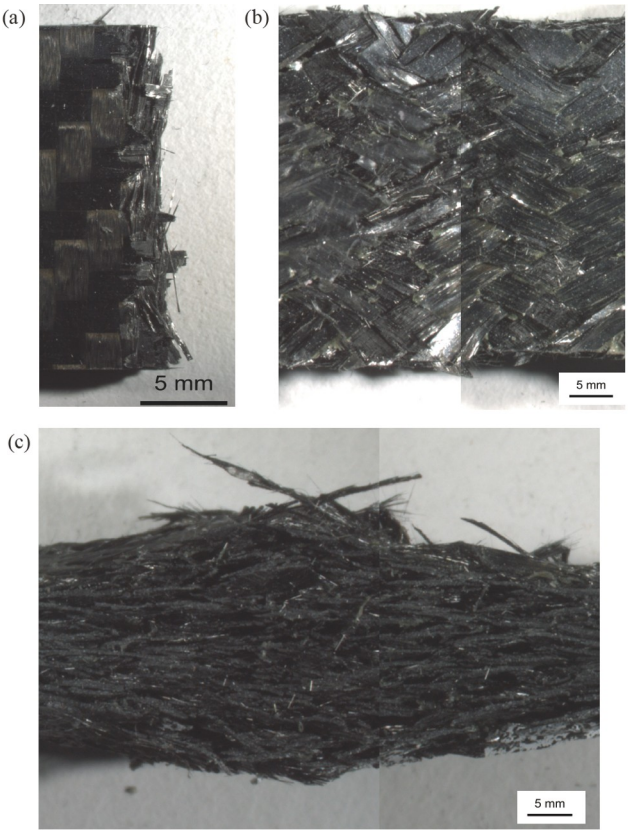

Figure 14 The images of destructed specimens: (a) Type-0; (b) Type-45 on top of, (c) Type-45 on the side.

Conflict of interest *On behalf of all authors, the corresponding author states that there is no conflict of interest.*

Author contributions *Valeriy Wildemann designed and fully supported the research (Conceptualization, Funding acquisition, Methodology, Resources, Project administration, Supervision, review & editing). Elena Strungar, Dmitrii Lobanov, Artur Mugatarov, and Ekaterina Chebotareva set up the experiment and processed the experimental data, wrote the first draft of the manuscript. (Formal analysis, Investigation, Writing – original draft). Elena Strungar and Ekaterina Chebotareva helped to organize the final version of the manuscript (Visualization). Elena Strungar, Dmitrii Lobanov, Artur Mugatarov, and Ekaterina Chebotareva revised and edited the final version (Writing – review & editing).*

Acknowledgements *This work was supported by the Russian Science Foundation (Grant No. 22-19-00765) at the Perm National Research Polytechnic University.*

1 K. Shirvanimoghaddam, K. V. Balaji, M. Ahmadi, H. Ajdari Nazarloo, R. Yadav, O. Zabihi, B. Egan, P. Adetunji, and M. Naebe, Strategies to resolve intrinsic conflicts between strength and toughness in polyethylene composites, Adv. Ind. Eng. Polym. Res. doi: 10.1016/j.aiepr.2023.03.004 (2023).
2 S. Rouf, A. Raina, M. Irfan Ul Haq, N. Naveed, S. Jeganmohan, and A. Farzana Kichloo, 3D printed parts and mechanical properties: Influencing parameters, sustainability aspects, global market scenario, challenges and applications, Adv. Ind. Eng. Polym. Res. **5**, 143 (2022).
3 X. Wang, H. Yuan, Y. Pan, C. Liu, C. Shen, and X. Liu, Creep behavior and mechanical properties of isotactic polypropylene composites via twice melt injection molding, Adv. Ind. Eng. Polym.

Res. **2**, 102 (2019).
4 E. Sparnins, and J. Andersons, Modeling the nonlinear deformation of composite laminates based on plasticity theory, Mech. Compos. Mater. **43**, 203 (2007).
5 M. Vogler, R. Rolfes, and P. P. Camanho, Modeling the inelastic deformation and fracture of polymer composites—Part I: Plasticity model, Mech. Mater. **59**, 50 (2013).
6 I. R. Cózar, F. Otero, P. Maimí, E. V. González, S. Miot, A. Turon, and P. P. Camanho, A three-dimensional plastic-damage model for polymer composite materials, Compos. Part A: Appl. Sci. Manuf. **163**, 107198 (2022).
7 Y. V. Sokolkin, and V. Vil'deman, Post-critical deformation and failure of composite materials, Mech. Compos. Mater. **29**, 120 (1993).
8 V. E. Wildemann, On the solutions of elastic-plastic problems with contact-type boundary conditions for solids with loss-of-strength zones, J. Appl. Math. Mech. **62**, 281 (1998).
9 M. G. Chausov, P. O. Maruschak, V. Hutsaylyuk, L. Śnieżek, and A. P. Pylypenko, Effect of complex combined loading mode on the fracture toughness of titanium alloys, Vacuum **147**, 51 (2018).
10 N. G. Chausov, D. G. Voityuk, A. P. Pilipenko, and A. M. Kuz'menmenko, Setup for testing materials with plotting complete stress-strain diagrams, Strength Mater. **36**, 532 (2004).
11 H. Talebi, M. Silani, S. P. A. Bordas, P. Kerfriden, and T. Rabczuk, A computational library for multiscale modeling of material failure, Comput. Mech. **53**, 1047 (2014).
12 M. A. Msekh, N. H. Cuong, G. Zi, P. Areias, X. Zhuang, and T. Rabczuk, Fracture properties prediction of clay/epoxy nanocomposites with interphase zones using a phase field model, Eng. Fract. Mech. **188**, 287 (2018).
13 N. Vu-Bac, T. Lahmer, X. Zhuang, T. Nguyen-Thoi, and T. Rabczuk, A software framework for probabilistic sensitivity analysis for computationally expensive models, Adv. Eng. Softw. **100**, 19 (2016).
14 H. Dang, P. Liu, Y. Zhang, Z. Zhao, L. Tong, C. Zhang, and Y. Li, Theoretical prediction for effective properties and progressive failure of textile composites: A generalized multi-scale approach, Acta Mech. Sin. **37**, 1222 (2021).
15 A. Fedorenko, B. Fedulov, Y. Kuzminova, S. Evlashin, O. Staroververov, M. Tretyakov, E. Lomakin, and I. Akhatov, Anisotropy of mechanical properties and residual stress in additively manufactured 316 L specimens, Materials **14**, 7176 (2021).
16 S. Fomin, Y. Izbash, Y. Bondarenko, S. Butenko, and I. Plakhotnikova, Complete "stress-strain" diagrams of rolled steal beams, MATEC Web. Conf. **230**, 02008 (2018).
17 C. Y. Liu, Y. Wang, X. P. Zhang, and L. Z. Du, Rock brittleness evaluation method based on the complete stress-strain curve, Frat. Integr. Strut. **13**, 557 (2019).
18 A. I. Chanyshev, and O. E. Belousova, Interpretation of zonal disintegration of the rock mass around openings, Phys. Mesomech. **12**, 89 (2009).
19 X. Yang, T. Wu, and X. Liu, Stress-strain model for lightweight aggregate concrete reinforced with carbon-polypropylene hybrid fibers, Polymers **14**, 1675 (2022).
20 R. Zhang, L. Guo, and W. Li, Combining thermal loading system with acoustic emission technology to acquire the complete stress-deformation response of plain concrete in direct tension, Materials **14**, 602 (2021).
21 M. Zhao, B. Zhang, P. Shang, Y. Fu, X. Zhang, and S. Zhao, Complete stress-strain curves of self-compacting steel fiber reinforced expanded-shale lightweight concrete under uniaxial compression, Materials **12**, 2979 (2019).
22 A. Pantano, Cohesive model for the simulation of crack initiation and propagation in mixed-mode I/II in composite materials, Appl. Compos. Mater. **26**, 1207 (2019).
23 X. Lu, M. Ridha, B. Y. Chen, V. B. C. Tan, and T. E. Tay, On cohesive element parameters and delamination modelling, Eng. Fract. Mech. **206**, 278 (2019).
24 H. Xie, L. Zhang, X. Sun, X. Wang, and Y. Cao, Tensile failure characteristics of coal and its 3D cohesive zone model, Geotech. Geol. Eng. **41**, 2299 (2023).
25 N. P. Semenyuk, and V. M. Trach, Stability and postcritical behavior of cylindrical composite shells with local imperfections under external pressure, Int. Appl. Mech. **52**, 624 (2016).
26 P. P. Camanho, C. G. Davila, and M. F. de Moura, Numerical simulation of mixed-mode progressive delamination in composite materials, J. Compos. Mater. **37**, 1415 (2003).
27 A. Beghini, Z. P. Bažant, A. M. Waas, and S. Basu, Postcritical imperfection sensitivity of sandwich or homogenized orthotropic columns soft in shear and in transverse deformation, Int. J. Solids Struct. **43**, 5501 (2006).
28 D. S. Lobanov, O. A. Staroverov, and M. P. Tretyakov, Realization effects of postcritical deformation the regularities for GFRP in tensile tests, IOP Conf. Ser.-Mater. Sci. Eng. **747**, 012120 (2020).
29 M. P. Tretyakov, D. S. Lobanov, and V. E. Wildemann, Study of the regularities of postcritical behavior and failure of specimens in the tests of composite materials, Procedia Struct. Integrity **17**, 865 (2019).
30 W. Van Paepegem, I. De Baere, and J. Degrieck, Modelling the nonlinear shear stress-strain response of glass fibre-reinforced composites. Part I: Experimental results, Compos. Sci. Tech. **66**, 1455 (2006).
31 R. M. O'Higgins, C. T. McCarthy, and M. A. McCarthy, Identification of damage and plasticity parameters for continuum damage mechanics modelling of carbon and glass fibre-reinforced composite materials, Strain **47**, 105 (2011).
32 J. H. Choi, J. Jang, W. Shim, J. M. Cho, S. J. Yoon, C. H. Choi, H. N. Han, and W. R. Yu, Determination of the in-plane shear modulus of unidirectional carbon fiber-reinforced plastics using digital image correlation and finite-element analysis, Compos. Struct. **229**, 111392 (2019).
33 Y. Liang, H. Wang, and X. Gu, In-plane shear response of unidirectional fiber reinforced and fabric reinforced carbon/epoxy composites, Polym. Test. **32**, 594 (2013).
34 V. G. Bazhenov, S. L. Osetrov, and D. L. Osetrov, Analysis of regularities of stretching of elastoplastic specimens and formation of a neck taking into account edge effects, Appl. Mech. Tech. Phys. **59**, 133 (2018).
35 M. P. Tretyakov, T. V. Tretyakova, and V. E. Wildemann, Regularities of mechanical behavior of steel 40Cr during the postcritical deformation of specimens in condition of necking effect at tension, Frat. Integr. Strut. **12**, 146 (2018).
36 V. Wildemann, O. Staroverov, E. Strungar, E. Lunegova, and A. Mugatarov, Stability of postcritical deformation of CFRP under static ±45° tension with vibrations, Polymers **14**, 4502 (2022).
37 V. Wildemann, O. Staroverov, E. Strungar, A. Mugatarov, and A. Kuchukov, Mechanical properties degradation of fiberglass tubes during biaxial proportional cyclic loading, Polymers **15**, 2017 (2023).
38 M. Gljušćić, M. Franulović, D. Lanc, and Ž. Božić, Application of digital image correlation in behavior modelling of AM CFRTP composites, Eng. Fail. Anal. **136**, 106133 (2022).
39 E. M. Strungar, A. S. Yankin, E. M. Zubova, A. V. Babushkin, and A. N. Dushko, Experimental study of shear properties of 3D woven composite using digital image correlation and acoustic emission, Acta Mech. Sin. **36**, 448 (2020).
40 D. Xu, C. Cerbu, H. Wang, and I. C. Rosca, Analysis of the hybrid composite materials reinforced with natural fibers considering digital image correlation (DIC) measurements, Mech. Mater. **135**, 46 (2019).
41 M. Azadi, M. Saeedi, M. Mokhtarishirazabad, and P. Lopez-Crespo, Effects of loading rate on crack growth behavior in carbon fiber reinforced polymer composites using digital image correlation technique, Compos. Part B-Eng. **175**, 107161 (2019).
42 E. Strungar, D. Lobanov, and V. Wildemann, Evaluation of the sensitivity of various reinforcement patterns for structural carbon fibers to open holes during tensile tests, Polymers **13**, 4287 (2021).
43 M. Pankow, B. Justusson, M. Riosbaas, A. M. Waas, and C. F. Yen, Effect of fiber architecture on tensile fracture of 3D woven textile

composites, Compos. Struct. **225**, 111139 (2019).
44 S. Han, Y. He, J. Lei, Y. Xie, and Y. Yang, A strain mode spectral digital image correlation method for displacement field analysis, Acta Mech. Sin. **39**, 422430 (2023).
45 M. Šofer, P. Šofer, M. Fusek, J. Cienciala, and P. Kwiatoń, Adaptive approach methodology of the Ib-value estimator calculation for acoustic emission analysis of carbon fibre reinforced plastics, Eng. Fail. Anal. **149**, 107264 (2023).
46 E. Uhlmann, and T. Holznagel, Acoustic emission-based process monitoring in the milling of carbon fibre-reinforced plastics, CIRP J. Manuf. Sci. Tech. **37**, 464 (2022).
47 W. Zhao, N. Pei, and C. Xu, Experimental study of carbon/glass fiber-reinforced hybrid laminate composites with torsional loads by using acoustic emission and micro-CT, Compos. Struct. **290**, 115541 (2022).
48 G. Yong, X. Denghong, H. Tian, L. Ye, L. Naitian, Y. Quanhong, and W. Yanrong, Identification of damage mechanisms of carbon fiber reinforced silicon carbide composites under static loading using acoustic emission monitoring, Ceram. Int. **45**, 13847 (2019).
49 D. E. Mouzakis, and D. G. Dimogianopoulos, Acoustic emission detection of damage induced by simulated environmental conditioning in carbon fiber reinforced composites, Eng. Fract. Mech. **210**, 422 (2019).
50 K. Asamene, L. Hudson, and M. Sundaresan, Influence of attenuation on acoustic emission signals in carbon fiber reinforced polymer panels, Ultrasonics **59**, 86 (2015).
51 V. Arumugam, K. Saravanakumar, and C. Santulli, Damage characterization of stiffened glass-epoxy laminates under tensile loading with acoustic emission monitoring, Compos. Part B-Eng. **147**, 22 (2018).
52 C. Barile, C. Casavola, G. Pappalettera, and P. K. Vimalathithan, Damage characterization in composite materials using acoustic emission signal-based and parameter-based data, Compos. Part B-Eng. **178**, 107469 (2019).
53 E. M. Strungar, and D. S. Lobanov, Development of the digital image correlation (DIC) method for mechanical testing at elevated temperatures, PNRPU Mech. Bull. **3**, 147 (2022).
54 A. A. Bryansky, O. V. Bashkov, I. V. Belova, and T. I. Bashkova, Investigation of damages formed in polymer composite materials under bending loading and their identification by the acoustic emission technique, Front. Mater. Technol. **2**, 7 (2022).
55 J. Xu, S. Ashraf, S. khan, X. Chen, A. Akbar, and F. Farooq, Micro-cracking pattern recognition of hybrid CNTs/GNPs cement pastes under three-point bending loading using acoustic emission technique, J. Building Eng. **42**, 102816 (2021).
56 K. Bhaskar, and T. K. Varadan, Theory of Isotropic/Orthotropic Elasticity (Springer, Cham, 2022).

基于数字图像相关和声发射技术的层状复合材料拉伸后临界变形阶段实现的实验研究

Valeriy Wildemann, Elena Strungar, Dmitrii Lobanov, Artur Mugatarov, Ekaterina Chebotareva

摘要 在可预测的情况下, 实现损伤累积平衡过程的条件能够控制关键状态下结构元件的失效. 这提高了安全性, 并降低了事故中灾难性行为发生的概率. 在某些情况下, 平衡损伤累积会导致材料应力-应变曲线上的下落区(称为后临界阶段). 为了评估复合材料结构的强度和变形极限, 必须考虑这一点. 本文使用数字图像相关方法、声发射信号记录和光学显微镜研究了正交铺设复合材料在不同方向上拉伸至各向同性轴时的变形和失效过程, 提出了平面应力条件下复合材料的弹塑性变形模型, 分析了应变场的演化和颈缩的形成, 描述了后临界变形过程的阶段划分, 研究了测试期间获得的声发射信号, 定义了材料的特征损伤类型, 得出在结构强度分析中考虑聚合物复合材料后临界变形阶段的合理性和必要性的结论.